國立臺灣大學電機資訊學院光電工程學研究所

碩士論文

Graduate Institute of Photonics and Optoelectronics

College of Electrical Engineering and Computer Science

National Taiwan University

Master Thesis

利用飛秒聲學量測原子級界面層之彈性性質

Probing Elastic Properties of Atomically-thin Interfacial Layer by Femtosecond Acoustics

陳薈元

Hui-Yuan Chen

指導教授：孫啟光 博士

Advisor: Chi-Kuang Sun, Ph.D.

中華民國 104 年 7 月

July 2015

誌謝

能完成這篇論文，首先感謝我的指導教授孫啟光博士，老師對物理的直覺著實令人敬佩，悉心的教導也讓我一窺聲子領域的奧秘，不時的討論將我帶往正確的方向，使我在這三年中獲益良多。老師對於學術倫理的嚴謹要求更是我學習的典範。本論文的完成另外亦特別感謝臺大材料工程研究所陳敏璋教授的幫忙，以及施奐宇學長的大力協助。品質優良、厚度精準的氧化鋁薄膜幫助我獲得寶貴的實驗資料，使得本論文能夠更完整而嚴謹。

感謝剛進實驗室時，宏賓學長、怡如學姊和思齊學長耐心的指導我架設雷射光路以及各種做實驗的原則與觀念，讓我能在最短的時間內跟上實驗室的研究腳步；感謝昱傑、建誠學長雖不在實驗室，卻仍耐心與我通信，對我第一個研究題目上助益良多；感謝 Pierre-Adrien、郁儒學長在我無論實驗上或研究上遇到各種困難時，都不厭其煩地給予我最大的幫助，也為我未來的研究生涯豎立了良好的榜樣；感謝易浚總是那麼的有個性，給實驗室帶來許多趣味，也讓我的碩士生涯多了幾分歡樂；感謝健銘與我一起修習孫老師的固態雷射與非線性光學，每當跟你討論課程內容、解決作業時總是特別起勁，與你辯論、探導物理真的是非常享受；感謝明容學姐在我剛進實驗室的時候，就每天在 BLB 忙到很晚，讓我深刻明白這實驗室的強度；感謝宇翔學長化身超強助教，出題與閱卷都十分精實，讓我明白物理兼具靈活與精準；感謝子芳學姐的健談，也給了我很多在這實驗室的寶貴經驗；感謝又誠學長對於我未來的申請學校上給了許多的寶貴建議；感謝從前的交大學妹孟愉，妳認真做研究的進步速度，也是督促我趕快畢業的動力；感謝思宇，與你打網球和討論 POI 真是非常舒壓,而你遙不可及的車尾燈也是領我向前的燈塔；另外，要特別感謝郁儒與思齊學長，你們總在我迷失方向時關心我、拉我一把，讓我能完成本篇論文，順利畢業，謝謝你們。當然還要感謝助理 Rebecca，除了實驗室裡各種報帳與大小事務上的大力協助外，您還總是記得我們大家的生日，並給予最精心的驚喜。

三年裡的日子，實驗室生活的點點滴滴，都是值得珍藏的回憶；我想我會懷念每天中午吃118巷的pattern，還有聚餐總吃不膩的胖子小吃，以及新生南路旁那幾間Belgium Beer。與實驗室的各位能在匆忙的人生中短暫相會，實為寶貴的緣分；事實上，要感謝的人、要感謝的話太多了，以上僅略為簡述，希望沒有遺漏。最後，感謝我親愛的家人在這三年內的所有幫助，並且在我延畢時給予體諒與支持，謹以此論文獻給你們。

中文摘要

　　隨著現今高科技半導體製程持續朝著微縮的方向發展，各種先進製程設計出更複雜的堆疊結構、更稠密的材料組合，以期達到最高空間利用而增進元件整體的效能。在這樣的趨勢下，材料與材料間的界面數量相較以往大幅增加；然而，很多證據都顯示，在兩個異質材料間往往會有一層接近原子層級厚度(約 0~3 奈米)的界面層產生。我們認為此界面層之存在可能會改變兩兩材料間的熱傳導，進而影響元件的效能與可靠度；由於熱效應會隨元件尺寸愈小而愈發彰顯，此界面層的存在對於元件散熱的潛在影響更是不容忽視，因此成了我們主要研究的對象。在半導體材料中，熱主要是藉由聲學聲子之運動而傳遞。由於聲學聲子本質上就是固體材料中的彈性波，因此元件材料的彈性性質（如：聲阻抗、彈性係數等）便是了解聲子在材料中傳遞行為的關鍵，也成了處理元件散熱問題的重要資訊。然而，據我們所知，常見用於量測極薄材料之彈性性質的技術如：奈米壓痕技術、雷射表面聲波技術、表面布里淵散射技術等，都無法量測前述如此薄之界面層之彈性性質。而在此論文中，我們提出並示範飛秒聲學是一個有效量測此原子級厚度的界面層彈性性質的技術。

我們首先設計並建立了一個界面層模型系統(其結構為:氮化鎵/界面層/氧化鋁)，經由電子顯微鏡確認，其中的界面層約為 5~6 層原子層，厚度為 1.85 奈米。接著，我們利用飛秒超聲學技術的高空間與時間解析力，成功量測出此界面層的兩項彈性參數：聲阻抗與彈性係數。最後，我們簡單探討了此界面層之存在可能對於兩材料間熱能傳遞上的影響，以呼應我們的研究初衷。

從我們的研究可顯示，飛秒聲學技術是一種合適的方式來偵測原子級薄的界面層之彈性性質，提供了研究熱傳導所需的材料參數，對於為未來解決奈米元件散熱問題可說是重要的一步。

關鍵字：飛秒聲學、界面層、彈性係數、聲學阻抗、聲子、熱傳導

ABSTRACT

While the developing trend of modern electronic devices is toward scaling down, heat removal is a critical issue since thermal effect becomes seriously significant as dimensions shrink. Besides, many complex and denser structures such as 3D integrated circuits or FinFET were designed to exploit the limited space and optimize the overall device performance, which is a trend well-characterized by Moore's law. However, it is well-known that an interfacial layer (IL) is usually formed between two adjacent heterogeneous materials. The existence of this unavoidable interfacial layer might hinder the heat conduction in those fabricated devices, and thus certainly diminishes their operational lifetime. Since heat is mainly carried by acoustic phonons, elastic property of materials is among the essential information for thermal management. Unfortunately, a proper technology to probe the elastic property of this atomically-thin interfacial layer has not yet been documented.

In this thesis, we designed an interfacial layer (IL) model system between bulk GaN and Al_2O_3 film, and conducted femtosecond acoustic measurement to obtain the elastic properties of the IL. The acoustic impedance, mass density and a cross-plane elastic constant of the IL were successfully obtained. We further evaluated a 16% reduction in thermal energy transmission owing to the IL from a theoretical calculation.

With the capability of probing the elastic properties across layers of only several atoms thick, our demonstration could be deemed as the first step to deal with heat dissipation issue stemming from the ILs. Hopefully, our approach will provide a better thermal management for nano-scaled devices in the future.

Keywords: interfacial layer, elastic property, femtosecond acoustics, phonon, thermal management.

CONTENTS

LIST OF FIGURES

LIST OF TABLES

Chapter 1　Introduction

1.1. Motivation

The developing trend of modern electronic devices is to scale down to optimize their performance and reliability, promising us a more convenient life. While the electronic properties of those novel devices have been investigated intensively, the difficulty in heat removal is another critical issue since thermal effect becomes seriously significant as dimensions shrink [1, 2]. Moreover, many associations of materials and complex structures such as 3D integrated circuits or FinFET were designed to exploit the limited space and maximize the overall device performance, which is a trend well-characterized by Moore's law [3]. The versatile combination and stacking of materials lead to much more interfaces than the devices before. However, it is well-known that an interfacial layer (IL) is usually formed between two adjacent heterogeneous materials. Since its thickness is only several nanometers, such an IL was hard to detect and usually omitted before. However, with the help of element-sensitive technique like X-ray photoelectron spectroscopy (XPS) and the direct-imaging using Transmission Electron Microscopy (TEM), evidences of the existence of ILs are revealed and reported a lot [4-12]. The existence of this unavoidable interfacial layer might hinder the heat conduction in those nanoscale devices fabricated, and thus probably diminishes their operational lifetime.

In semiconductors, heat energy is mainly carried by acoustic phonons, which are categorized as one branch of phonons and are basically propagating elastic waves, or sound waves, in solids [13]. Therefore, the elastic properties of materials would provide us better knowledge of the behaviors of heat waves in semiconductor solids. In addition, elastic constant is one of the essential parameters required for constructing the interatomic potentials in molecular dynamics (MD) simulation of thermal conduction in

solids [14, 15]. Therefore, the elastic information of materials is essential for thermal management studies of semiconductor devices. Recalling our concern that the heat conduction in nanoscale materials would be affected due an inevitably-formed interfacial layer (IL), techniques to probe the elastic properties of an IL down to several nanometers are thus needed.

1.2. Existing Techniques

Several techniques which can probe the mechanical or elastic properties of thin-layers down to the nanometer scales have been reported. For example, nano-indentation, laser acoustic wave, and surface Brillouin scattering detection. Below, we briefly introduce them and discuss about their capabilities.

Nano-indentation (NI) is a well-developed and commercialized technique for quick measurement of the elastic properties of nanoscale thin films. An indenter (usually a tip) with a known geometry is used to create "indents" (tiny holes) on the sample. In the process of indenting, the normal force exerted on the tip and the depth of its penetration into the specimen are simultaneously recorded. After that, the elastic properties of the materials can be extracted by fitting the so-called load-displacement curve. However, despite of its convenience and speed, the NI measurement is apparently destructive. Besides, the depth of indents in a normal NI test should be less than 1/10 of the film thickness in order to be free from the influence of substrate. This requirement thus limits the film thickness to the range of tens of nanometers [16, 17].

Compared to the destructive character of NI, laser acoustic wave (LAW) method, also known as laser-induced surface acoustic wave technique (LISAW), is a non-destructive way to obtain the elastic properties of thin layer down to nanometers [18-20]. Through measuring the dispersion curve of the laser-generated surface acoustic waves (SAW) propagating parallel to the sample surface, the elastic properties can be determined.
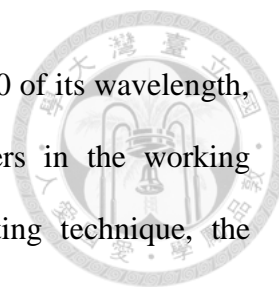
However, since the penetration depth of SAW is approximately 1/100 of its wavelength, the thickness is limited to about tens to hundreds of nanometers in the working frequency range 0.1~0.2GHz of SAW. With a sophisticated fitting technique, the thickness could be down to roughly below ten nanometers[19].

Surface Brillouin scattering (SBS) is a technique similar to LAW, which also obtains elastic properties of thin films using SAW. The only difference is in the detection method. Instead of using ultrasonic transducers as in LAW, SBS exploit laser detection which obtains the velocity of SAW by analysis the optical reflection spectrum [21, 22]. However, SBS suffers from same limitation due to the penetration depth of SAW.

We briefly listed some advantages, disadvantages and limitations of the techniques discussed above for a clearer comparison, as shown in Table.1.1. Please note that the thinnest layer reported among these techniques is 7.6nm by the laser acoustic wave technique [19]. However, the ILs are usually found to be below tens of atoms thick (0~3nm, estimated from Ref. [4-12]). Therefore, the necessity of a proper technique to probe the elastic property of atomically-thin IL stands for itself. In this thesis, we proposed that femtosecond acoustics is a suitable technique to probe the elastic properties of an atomically-thin interfacial layer.

Table 1.1

Comparison of several techniques for measuring the mechanical properties of materials.

Technique	Advantage	Disadvantage	Lowest thickness	Limitation
Nanoindentation	Fast	Destructive, surface layer	~ tens of nm	1/10 of indents
Laser Acoustic Wave	Non-destructive, opaque material	Surface layer	7.6 nm [19]	1/100 of SAW wavelength
Surface Brillouin Scattering	Non-destructive	Surface layer, Transparent material	~ <10 nm [20]	1/100 of SAW wavelength
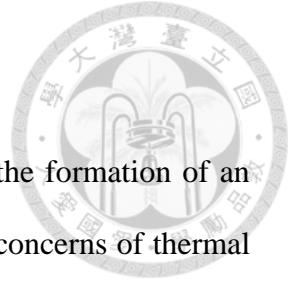
1.3. Thesis Scope

In Chapter 1, we briefly introduced a well-known phenomenon of the formation of an interfacial layer (IL) between two heterogeneous materials, and the concerns of thermal management were also addressed. Then, in Chapter 2, we introduced the basic physical principle of femtosecond acoustics from generation to detection mechanism of femtosecond acoustic phonon pulses. In Chapter 3, we designed an interfacial layer model system and conducted femtosecond acoustic experiment on the model system. Moreover, we demonstrated the successful investigation of the elastic properties of an IL with a thickness below 2 nm, while its acoustic impedance and elastic constant were obtained. In the final chapter, we gave a summary and the future prospective of this work.

Chapter 2 Femtosecond Acoustics
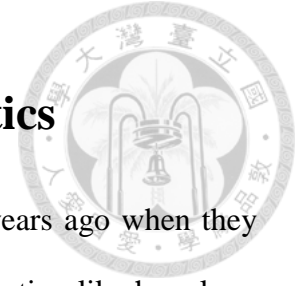
Humans have been very familiar with "echo" since thousands of years ago when they had discovered the returning sounds could bring back useful information like how long a cave is or how far a canyon is. Aftermath, sonic technique has been developed and applied in a variety of fields, such as the sonar system in naval research[23], ultrasonic imaging in medical application[24, 25], or nondestructive detection in architectural engineering[26]. Nowadays, as new techniques probing material properties under a nano-scale has become the spotlights in every fields, "echo" is no absence. The basic idea of femtosecond acoustics technique, introduced in the following content of this chapter, resembles to the traditional sonar technology. We generate acoustic waves propagating toward an unknown specimen, and then analyze the echoes to obtain the physical properties of the specimen (see Fig. 2.1). The major difference is that the sound waves generated in our technique are short acoustic pulses with full width at half maximum (FWHM) only hundreds of femtosecond (fs) in time domain, which allow us a high temporal resolution as well as a spatial one.
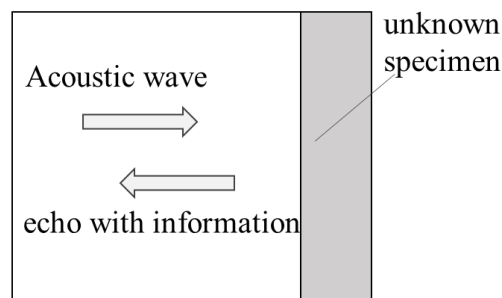
Fig. 2.1 Schematic diagram of a femtosecond acoustic measurement.

Following, we are going to briefly introduce some background knowledge of the femtosecond acoustics.
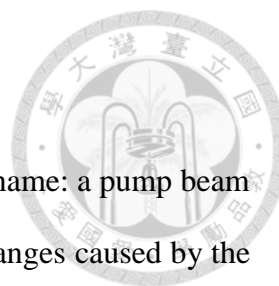
2.1 Pump-Probe Technique

The genera idea of a pump-probe experiment is pretty clear as in its name: a pump beam induces changes in the specimen, and a probe beam detects those changes caused by the pump with an adjustable time delay. The illustrated scheme of a typical transmission pump-probe measurement is depicted in Fig.2.2. The light source (could be a laser or an X-ray, etc.) is dived into a relatively intensive pump pulse and a much weaker probe pulse. The optical paths difference of the two pulses is controlled by a movable delay stage. These two beams are then focused with spatially overlapping onto the sample. The intensive pump pulse will transiently modify the optical property of the sample. Then, behind the sample, a photo-detector is used to record the optical change measured by the probe pulse. The delay stage which will move in a direction that delays the arriving time of probe pulse at the sample. In this way, a time-resolved transmission pump-probe experiment can be achieved.
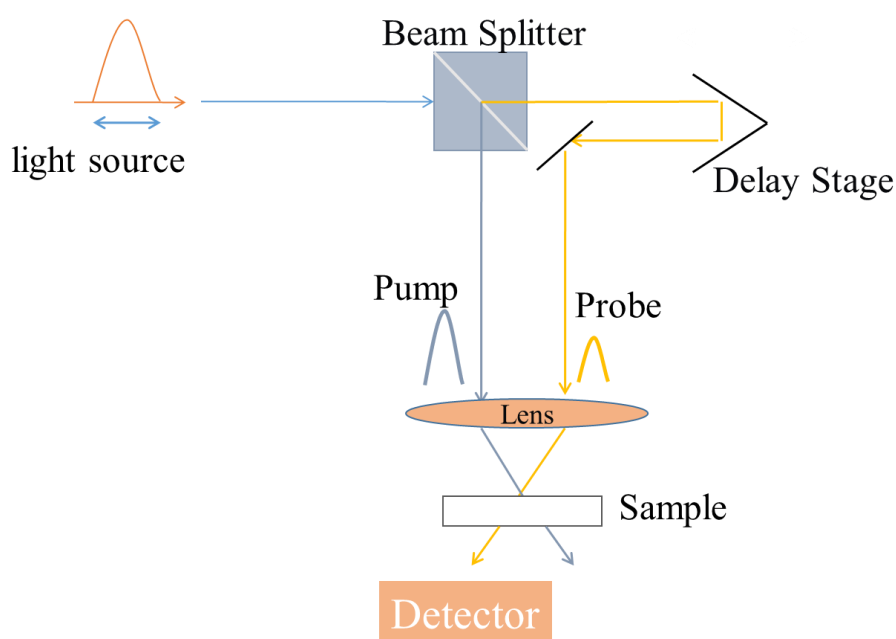
Fig. 2.2 Schematic diagram of a typical transmission pump-probe measurement.
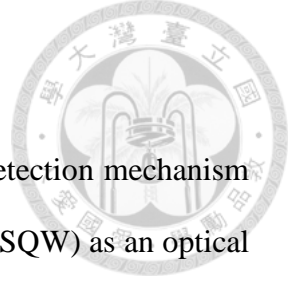
2.2 Femtosecond Acoustic Pulse

In this section, we are going to briefly explain the generation and detection mechanism of femtosecond acoustic pulse by empolying a single quantum well (SQW) as an optical piezoelectric transducer (OPT).

2.2.1 Generation Mechanism

The optical piezoelectric transducer (OPT) [27] we used in this thesis was a single strained-layer structure composed of a 3-nm InGaN layer embedded in bulk GaN, which thus formed a single quantum well (SQW) structure. Since GaN and InGaN are both piezoelectric materials, the existence of static strains at the boundary of GaN/InGaN due to lattice mismatch would result in strong built-in piezoelectric filed [28]. As depicted in Fig.2.3 (a), the built-in field, denoted as **E**, is responsible for the distorted band diagram. When a laser pulse incidented onto the SQW with a photon energy corresponding to the bandgap energy, carriers (i.e. electrons and holes) will be pumped to excited states (Fig.2.3 (b)). However, because of the high piezoelectric field and band-bending, those photo-excited carriers will be swept to different edges of the SQW (Fig.2.3 (c)). A new transient electric field **E'** is then formed due to this inhomogeneous spatial charge distribution (Fig.2.3 (d)), which immediately screens the original built-in piezoelectric field in the SQW (Fig.2.3 (e)). As a result, the lattice tends to relax to new equilibrium from the transient instability and releases the energy in the form of short acoustic phonon pulses (Fig.2.3 (f)). Detailed derivations of the mechanism using macroscopic continuum elastic theory can be found in Ref. [29].
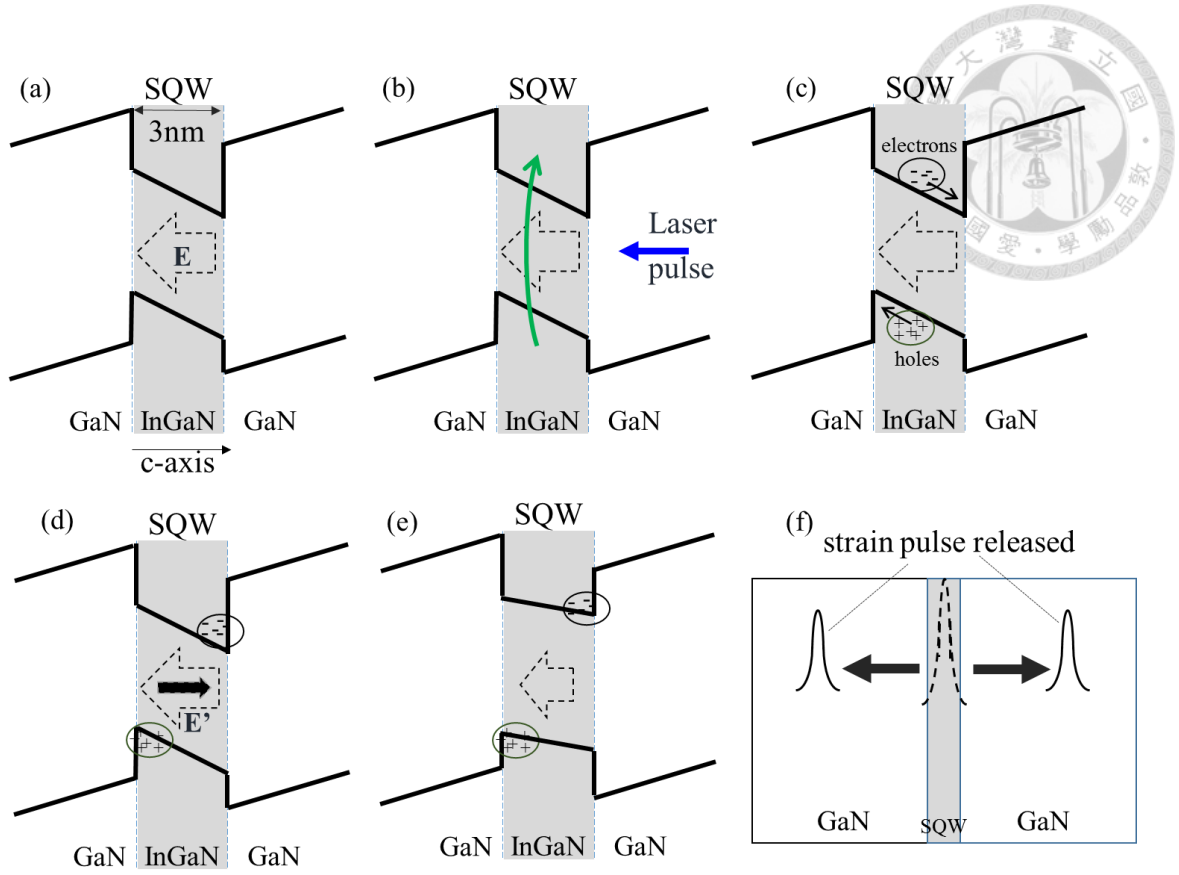
Fig. 2.3 Schematic flow charts for the generation mechanism of femtosecond acoustic phonon pulses. Description of (a)~(f) can be found in the text.

2.2.2 Detection Mechanism

The detection of femtosecond acoustic phonon pulses could be achieved by the very same OPT. Since acoustic pulses are basically propagating strain pulses inside solids, they could perturb the built-in piezoelectric field in the SQW when they pass through and thus result in modification of optical absorption by quantum-confined Franz-Keldysh (QCFK) effect[30]. The variation in optical transmission could be described as in [31]:

$$\left(\frac{\Delta T}{T}(t)\right) = \int_{-\infty}^{\infty} dz \, \Delta\alpha(z) = \int_{-\infty}^{\infty} dz \, s(z,t) \cdot F_{OPT}(z;\omega)$$

Eq. (2-1)

where $s(z,t)$ is the strain function and $F_{OPT}(z;\omega)$ is the sensitivity function by the QCFK effect, which could be calculated theoretically according to the structure of the OPT
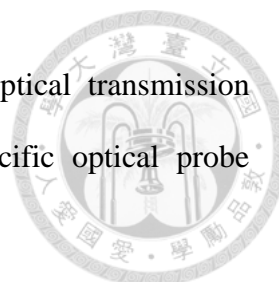
[31]. This sensitivity function contains the information of the optical transmission modulation strength resulting from the strain variation at a specific optical probe frequency ω.

The schematic diagram of the optical detection of femtosecond acoustic pulse is shown in Fig.2.4 (a). When using the SQW OPT as a detector for femtosecond acoustic pulse, the optical wavelength is chosen to be between the bandgap energy of the bulk material and the well (in our case, between GaN and InGaN). Thus the transient transmission of the optical probe will be strongly modulated while the acoustic pulses pass through the SQW.
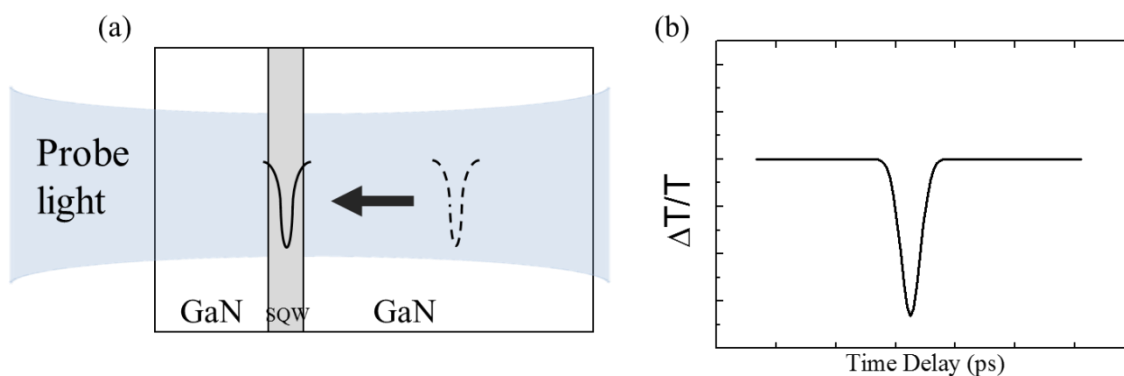
Fig. 2.4 (a) Schematic diagram of the optical detection of a femtosecond acoustic pulse using an OPT. (b) Schematic experimental trace of differentiated transmission changes, representing the detected femtosecond acoustic pulse.

2.3 Acoustic Reflection and Transmission

Since the acoustic phonons are basically elastic waves, or sound waves, in solids, we are going to introduce systematic description and phenomenal behaviors of elastic waves in this section. Using elastic wave theory, the reflection and transmission coefficients for acoustic waves are introduced.
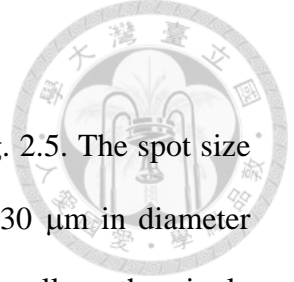
2.3.1 One-dimensional elastic waves

First, we set up the coordinates in for our sample as sketched in Fig. 2.5. The spot size of the laser to generate acoustic pulse in our experiment is about 30 μm in diameter while the spatial width of generated acoustic pulse is ~3nm as well as the single quantum well (SQW). It's noted that the dimension in the lateral (x and y) direction is far larger than in the axial (z) one. Therefore the acoustic pulse can be described as one dimensional elastic wave, where it satisfied the 1-D wave equation.
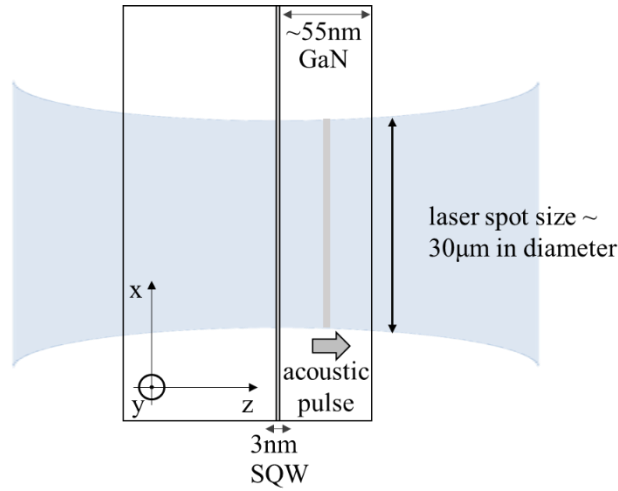
Fig. 2.5 Schematic diagram of the dimensions of our acoustic pulse system

2.3.2 Reflection and Transmission

From acoustic theory, the stress and particle velocity should be continue at the boundaries[32]. Using this criteria, the amplitude reflection and transmission coefficients for acoustic waves can be described as (from material 1 to 2):

$$r_{1\to2} = \frac{Z_2 - Z_1}{Z_1 + Z_2} \qquad t_{1\to2} = \frac{2Z_2}{Z_1 + Z_2}.$$

Eqs. (2-2)

In the notation, Z is an important elastic parameter called the acoustic impedance, and

$$Z_i = V_i \cdot \rho_i.$$

Eq. (2-3)

where V_i and ρ_i are the longitudinal sound velocity along z-direction and the mass density of the material i, respectively.

As for the power reflection and transmission, we first note that the energy flux carried by each acoustic wave is given by the Poynting vector, which is

$$P_i = \frac{\sigma_i^{\,2}}{Z_i}$$

where σ is the stress of the acoustic wave.

Therefore, the energy reflection and transmission coefficients from material 1 to material 2 will be

$$R_{0\rightarrow1} = \frac{(Z_0 - Z_1)^2}{(Z_0 + Z_1)^2} \qquad\qquad T_{0\rightarrow1} = \frac{4Z_0 Z_1}{(Z_0 + Z_1)^2}$$

Those formulas introduced above will be used in the analysis of our femtosecond acoustic signal in the following chapter.

Chapter 3

Model System for Probing Interfacial Layer

3.1 Experimental Design

3.1.1 Sample Preparation and Structure

First step, we designed the sample structure for our demonstration, which was a combination of GaN and Al_2O_3 with an atomically-thin interfacial layer. A detailed structure of the sample used in this thesis is sketched in figure 3.1. It is basically a 3-nm-thick [0001]-oriented Wurtzite $In_{0.14}Ga_{0.86}N$ embedded in-between a 3-mm-thick GaN buffer layer and a ~55-nm-thick GaN cap layer. This single quantum well (SQW) structure was for generation and detection of femtosecond acoustic phonon pulses, as introduced in Chapter 2. All of these three layers were grown by metal-organic chemical vapor deposition (MOCVD) on a double-polished c-plane sapphire substrate. Then, an 20.2-nm thick aluminum oxide (Al_2O_3) was grown on top of the GaN cap layer by a commonly-used technique called thermal atomic layer deposition (ALD)[33]. Water vapor and trimethylaluminum (TMA) were used as the two precursors for oxygen and aluminum [34]. Under a temperature of 200°C, a pressure of 0.5torr and pulse duration of 0.012s for each cycle, the average growth rate of is about 1.07 angstrom/cycle. After the ALD process, a 1.85nm-thick interfacial layer (IL) was inevitably formed amid GaN cap layer and the deposited Al_2O_3 film, which was later confirmed by high-resolution transmission electron microscopy (HRTEM), as shown in figure 3.2. Similar ALD procedure of exactly same substrate and grown material (GaN and Al_2O_3, respectively) was also reported with an interfacial layer [11]. These top-most three layers, i.e. GaN/IL/Al_2O_3, composed our model system. The sample was fabricated with the help of

Huan-Yu Shih from Prof. Miin-Jang Chen's laboratory in the Department of Materials Science and Engineering, National Taiwan University.
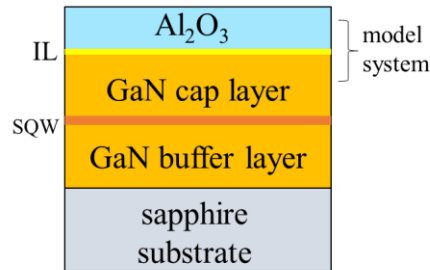
Fig. 3.1 Schematic diagram of the sample structure.
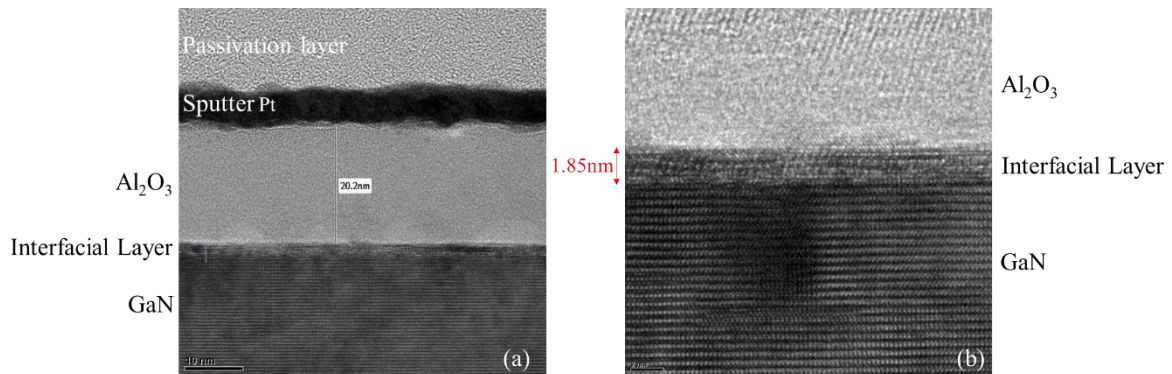
Fig. 3.2 Bright-field high-resolution transmission microscopy (HRTEM) image of our sample with different magnification, showing the existence of an interfacial layer between GaN and Al_2O_3. (a) 360 kx magnified (b) 930 kx magnified.

3.1.2 Setup and Measurement Details

We built up a typical one-color femtosecond pump-probe transient transmission setup at room temperature to perform our investigation, as depicted in Fig.3.3. A commercialized Kerr-lens mode-locked Ti:sapphire femtosecond laser with a repetition rate of 76 MHz and center wavelength at 800 nm was utilized as the light source for the measurement. Next, a 300-μm-thick beta barium borate (BBO) crystal was applied for the second harmonic generation (SHG) process to crease frequency-doubled ultraviolet (UV) light pulse that matched the bandgap energy of InGaN SQW. Behind a UV-color filter for extinction of unconverted red light, a polarizing beam splitter (PBS) was
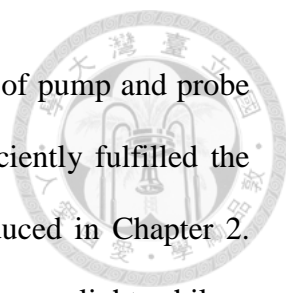
employed to divide the laser beam into an s-polarized pump beam and a p-polarized probe beam. In-between the UV-color filter and the beam splitter, we placed a half-wave plate for convenient modification of the pump/probe ratio. A high-resolution motorized linear translation stage equipped with a retro-reflector was introduced on the pump arm in an attempt to accurately control the optical path difference (OPD) between two arms, which corresponds to the time delay between pump and probe pulses. On the other arm, we set up a telescope for further improvement of the spatial overlapping of two beams and a neutral density (ND) filter wheel to ensure that the probe power was low enough not to affect the transient state pumped. The combined utilization of the half-wave plate and the ND filter wheel enabled us to individually adjust the power of pump beam and the probe beam. A pump power of 14 milliwatt (mW) and a probe power of 1.4mW were adopted during our experiment.
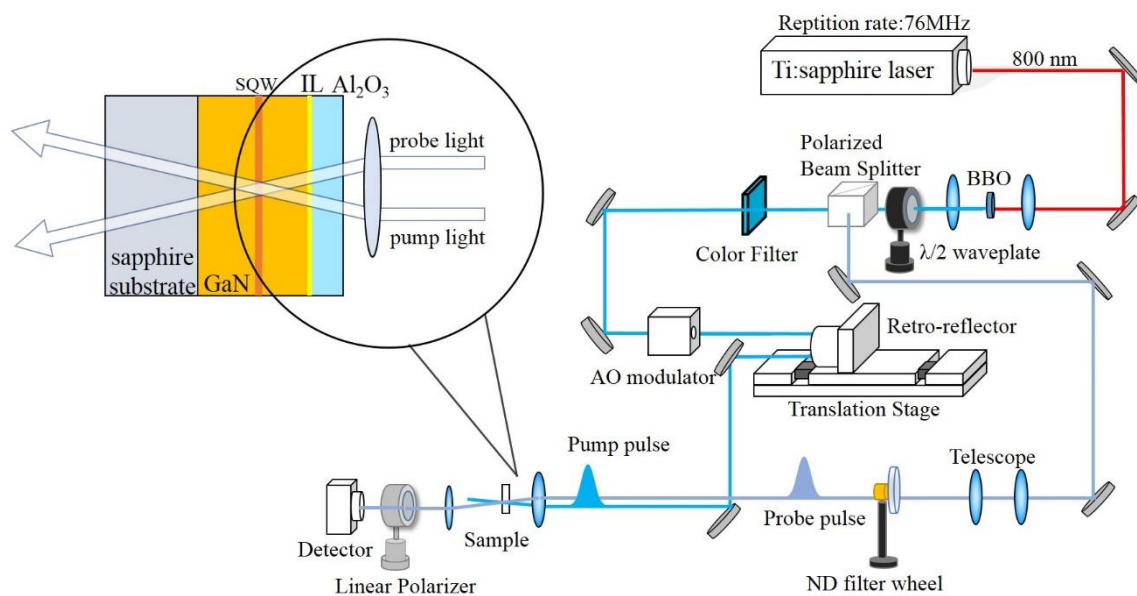
Fig. 3.3 The femtosecond pump-probe transient transmission measurement setup.

In the last part of the setup, two laser beams were aligned parallel before focused on the sample by an aspheric objective lens with a focal length of 0.5 cm. The position of the
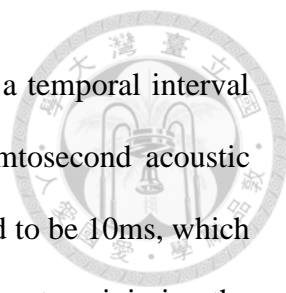
sample was optimized for the condition that the overlapped portion of pump and probe light were located right at the SQW inside the sample, which efficiently fulfilled the generation and detection of femtosecond acoustic pulses, as introduced in Chapter 2. Behind the sample, an iris was placed to block the scattering of pump light while a plane-convex lens was used to collect the diverging probe light and direct it into a high speed Si photodetector. The photodetector recorded the transmission intensity of the probe light and was put near but not at the lens' focal point so as not to be damaged. Moreover, to obtain a high signal-to-noise ratio (SNR) for our measurement, a linear polarizer was employed as the last component before the photodetector to eliminate any scattered s-polarized pump light.

Concerning the signal collecting method, a phase-sensitive detection was adopted with joined appliance of an acousto-optic modulator (AOM) and a RF lock-in amplifier. The AOM can modulate laser beams in much higher frequencies compared to conventional mechano-optical choppers, thus a higher SNR could be achieved due to the reduction of the pink noise (i.e. inverse-frequency noise). In our experiment, a 2MHz electrical square wave signal with 1V peak-to-peak value, 0.5V offset, and a 50% duty-cycle was produced by a function generator and sent to both AOM's controller and the reference port of the lock-in amplifier synchronously through low noise coaxial cables. The phased-locked signals were recorded by a LabVIEW program as a function of time delay between pump pulse and probe pulse.

For resolving phonon pulses with a FWHM ~600fs in our experiment, we set the moving speed of the translation stage and the sampling rate of lock-in amplifier to be 1.28mm/s and 128Hz, respectively. According to this pair of setting, an OPD of 0.02mm

(roundtrip) between each data point was realized, corresponding to a temporal interval ~66fs and an equivalent sampling frequency of 15THz for our femtosecond acoustic measurement. The time constant of the lock-in amplifier was selected to be 10ms, which was the only option closest to the sampling interval (~7.8ms), so as to minimize the sampling errors.

For the calibration of differentiated transmission changes ($\Delta T/T$), we need to measure the transmission (T) of the probe light as well. However, it will be of huge inconvenience to move the AOM back and forth between pump arm and probe arm because it will affect all the remaining system afterwards. Therefore, we used a movable mechanical chopper instead. Same transient transmission difference measurement like the use of AOM was conducted on the pump arm. For the transmission, the magnitude of the modulated probe beam was measured while the pump beam was blocked. Since we only need a ratio number, mechanical chopper had provided enough SNR for the calibration measurement.
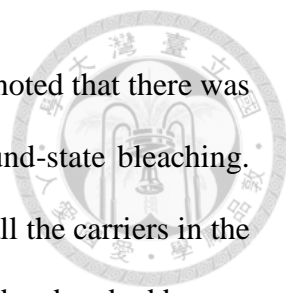
3.2 Experimental Results and Analysis

The proposed approach to characterize the interfacial layer is revealed in this section.

We showed the experimental results of one color (400 nm) pump-probe transient transmission measurement and our data analysis processes involving removing of background and calculation of elastic properties.

3.2.1 Background Signals

The magnitude of variation in optical signals due to phonons is usually around the order of 10^{-5}, relatively insignificant compared to other background in an optical experiment. Therefore, several steps of background removing were needed before obtaining our signals of interest. The measured transient differentiated transmission difference ($\Delta T/T$)

of our model interfacial system was shown in Fig. 3.4. It was firstly noted that there was a step-like rising in the transmission, which was the result of ground-state bleaching. Since the former intensive femtosecond pump pulse had stimulated all the carriers in the quantum well to excited states, the following probe would no longer be absorbed by any inter-band transition. Thus, the transmission of probe light across the sample suddenly increased. As a matter of fact, the point with the largest slope is usually defined to be the time zero of pump-probe delay, and so was it in this thesis. As the photo-excited carriers, i.e. electrons and holes, gradually recombined over time [35, 36], the transmission of delayed probe light started to decay exponentially after the step-like rising. This feature of rising and decaying, so called carrier dynamics, had been studied using pump-probe technique for decades in the characterization of tons of semiconductors and nanostructures[37]; however, it's not relevant to the main scope of this thesis. Therefore, here we simply used an exponential decay fitting to subtract this background, as the red solid line depicted in Fig. 3.4 (a). A lifetime of 143ps fitted was in good agreement with the reported value[35]. The residual signals containing a clear oscillation and successive echoes was then shown in Fig. 3.4 (b).
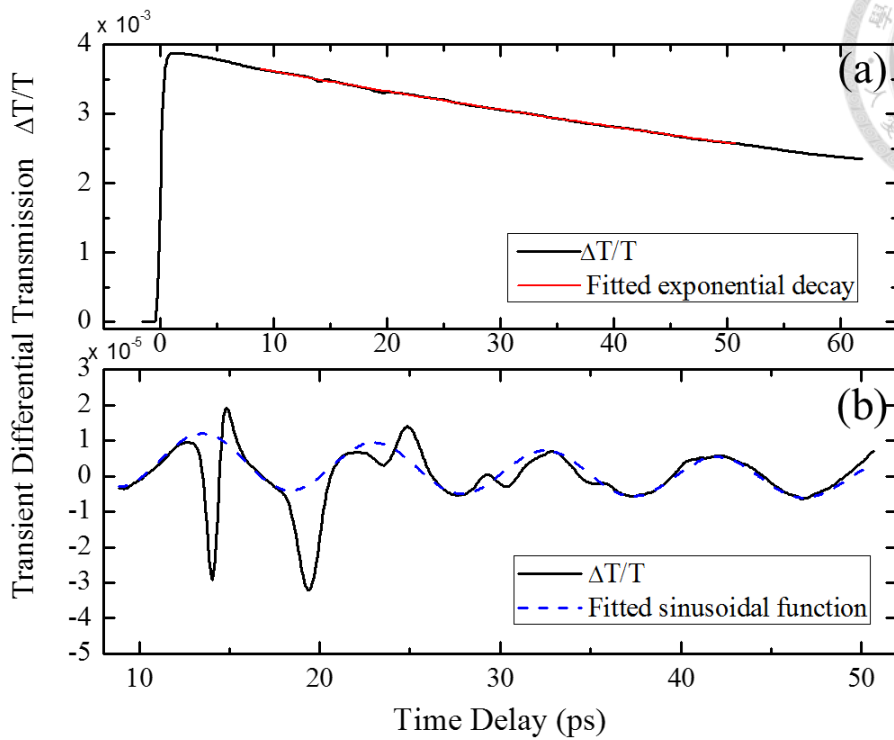
Fig. 3.4 Differentiated transmission changes ΔT/T of the experimental data (black solid),

double exponential fitting curve (red solid), and sinusoidal fitting curve (blue dash).

Both pump and probe wavelengths were 400nm.

The sinusoidal-like fluctuation was resulted from another phenomenon caused by the

scattering of incident photons and propagating acoustic phonons, known as the Brillouin

oscillation [38-44]. In a macroscopic point of view, when an acoustic pulse was induced

in a bulk solid, the optical properties of this material could be modulated owing to

photoelastic effect. The strain-induced local refractive index variation δn would act as a

moving reflective interface for the probe light. An illustrative sketch of this

circumstance was shown in Fig. 3.5. In fact, this arrangement was basically a dynamic

Fabry-Pérot cavity [42]. The maximum or minimum of optical transmission would

occur as long as the cavity length equaled to a multiple of half optical wavelength or an

odd multiple of quarter optical wavelength, respectively. As the cavity length changed

due to the moving phonon, an oscillation in the intensity of transmitted probe light was recorded as the sinusoidal background in our signals.
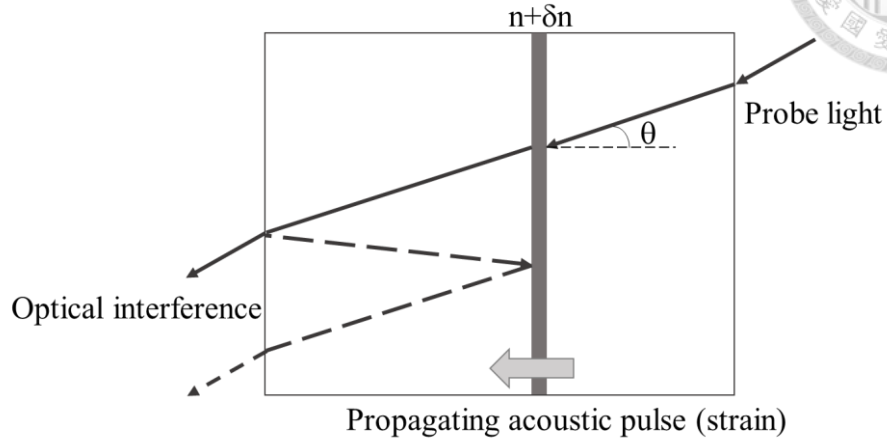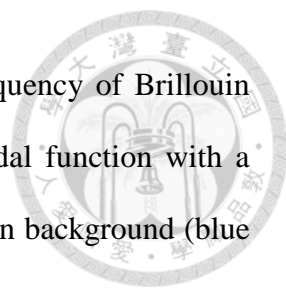
Fig. 3.5 Schematic illustration of strain-induced dynamic Fabry-Pérot effect, also called Brillouin oscillation. The dark area represents the propagating acoustic pulse, and the symbol δn denotes the refractive index variation.

As for the oscillation frequency, we can estimate it from the interference condition of the dynamic Fabry-Pérot cavity [42]; or, in a simple quantum-mechanical point of view: Only if the phase matching condition between photons and acoustic phonons was fulfilled would the reflection of incident light be maximized by the strain pulse[44]. Either way, the frequency could be calculated using the equation below:

$$f_{phonon} = \frac{2nV_{phonon}\cos\theta}{\lambda_{photon}} \quad , \qquad \text{Eq. (3-1)}$$

where f_{phonon} is the phonon frequency contributed to Brillouin oscillation, n is the optical refractive index, V_{phonon} is the longitudinal acoustic phonon velocity, θ is the incidence angle as denoted in Fig.3.5, and λ_{photon} is the optical probe wavelength.

In our experiment, the refractive index of GaN at the probe wavelength of 400 nm was 2.53 [45] and the longitudinal acoustic phonon velocity along c-axis (0001) was 7.96

nm/ps [46]. In a normal incidence arrangement, the calculated frequency of Brillouin oscillation was around 0.1 THz. Shown in Fig. 3.4 (b), a sinusoidal function with a frequency of 105 GHz was in a good fit with the Brillouin oscillation background (blue dash line).

Since Brillouin oscillation was the result of propagating phonons in bulk material, in a layered system, it might raise concerns that there should be more than one oscillation frequency in the signals because there were phonons in different materials, for example, IL and Al_2O_3 in our experiment. However, it was not observed in our experimental data. We supposed that it's because such oscillation with different frequencies and abrupt phase changes, in our case, should exist primarily before 14ps (the time that first echo came back and was detected by the SQW). After that, the phonon pulse in Al_2O_3 would had gone through several reflections that reduced its amplitude each time, causing its own Brillouin oscillation ignorable in the signals. As a matter of fact, the smooth and long-lasting oscillation observed in Fig.3.4 (b) was due to the phonon pulse propagating in the direction toward sapphire substrate, where it experienced low attenuation and no reflection for a considerable long time before arriving at the GaN/sapphire interface.

3.2.2 Acoustic Impedance and Elastic Constant Analysis

After carefully removing the carrier dynamics and Brillouin oscillation background, the echo signals became clearer. The background-free experimental data was revealed in Fig.3.6 (a), which was in fact a typical femtosecond acoustic A-scan of our sample. E1~E6 indicated each echo corresponding to different roundtrips inside Al_2O_3 film, as shown in the schematic diagram in Fig.3.6 (b).
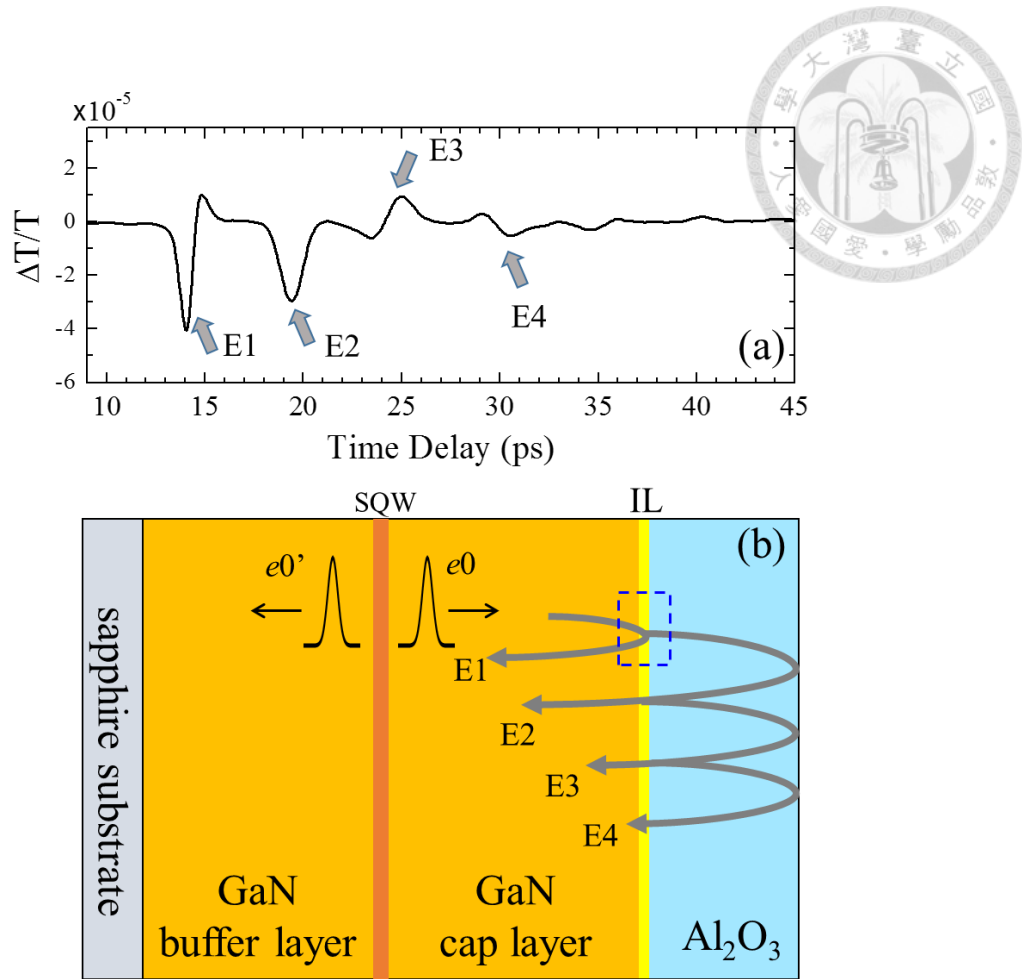
Fig. 3.6 (a) Background-free femtosecond acoustic A-scan signal of our sample. (b) Schematic diagram of the multiple echoes. Zoom-in diagram on the interfacial layer (blue dash frame) was shown in Fig.3.7.

We noted that the mechanical property of the IL was contained in the first echo E1 without the influence from additional propagation in Al_2O_3 film like in the other echoes. Thus it became our focus. Since the shape of our acoustic pulse source was Gaussian-like, the clear bi-polar profile of E1 certainly impled interference of echoes. Zoom-in signal and diagram of E1 was displayed in Fig.3.7. For analyzing the composition of E1, we employed a convolution fitting with a Gaussian pulse with two impulses to divide it into three echoes, denoted as e_1, e_2 and e_3. Corredponding trace diagram was sketched in Fig3.7 (b): e_0 was the acoustic pulse source; e_1 indicated the

echo reflected at GaN/IL interface; e_2 was the acoustic pulse that transmitted into IL, reflected at IL/Al_2O_3 interface, and then transmitted back into GaN; e_3 denoted the acoustic pulse with another additional roundtrip inside the IL. With the knowledge of their journeys, we could represent all e_1, e_1 and e_3 with e_0 using acoustic relflection and transmission theory[32]. As introduced in section 2.3, the expressions would be

$$e_1 = e_0 \cdot t_{0 \to 1} = e_0 \cdot \left(\frac{Z_1 - Z_0}{Z_1 + Z_0} \right),$$
Eq. (3-2)

$$e_2 = e_0 \cdot t_{0 \to 1} \cdot r_{1 \to 2} \cdot t_{1 \to 0} = e_0 \cdot \left(\frac{2Z_1}{Z_1 + Z_0} \right) \cdot \left(\frac{Z_2 - Z_1}{Z_2 + Z_1} \right) \cdot \left(\frac{2Z_0}{Z_1 + Z_0} \right),$$
Eq. (3-3)

$$e_3 = e_2 \cdot r_{1 \to 0} \cdot r_{1 \to 2} = e_2 \cdot \left(\frac{Z_0 - Z_1}{Z_1 + Z_0} \right) \cdot \left(\frac{Z_2 - Z_1}{Z_2 + Z_1} \right),$$
Eq. (3-4)

where $t_{i \to j}$ and $r_{i \to j}$ represent the amplitude transmission and reflection coefficients for acoustic wave propagating from material i to material j, respectively; Z_i is the characteristic acoustic impedance of the material i, by definition the product of mass density and sound velocity[32]. The subscript i (or j) is 0 for GaN, 1 for the IL, and 2 for Al_2O_3, as denoted in Fig.3.6 (b) and (c).

We further divided Eq. (3-3) by Eq. (3-2) and Eq. (3-4) by Eq. (3-3) to eliminate the source term e0, then we got
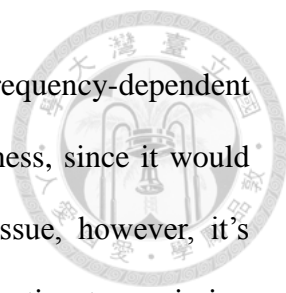
$$\frac{e_2}{e_1} = \frac{4 \cdot Z_0 \cdot Z_1 \cdot (Z_2 - Z_1)}{(Z_1 - Z_0)(Z_1 + Z_0)(Z_2 + Z_1)} \quad \text{and} \quad \frac{e_3}{e_2} = \left(\frac{Z_0 - Z_1}{Z_1 + Z_0} \right) \left(\frac{Z_2 - Z_1}{Z_2 + Z_1} \right).$$
Eqs. (3-5)

Since $e_1 \sim e_3$ are measured experimental results, Z_0 and Z_2 can be obtained from basic parameters of GaN and Al_2O_3, we can solve this equation to get the only one unknown variable Z_1, which would contain the mechanical information of the IL.
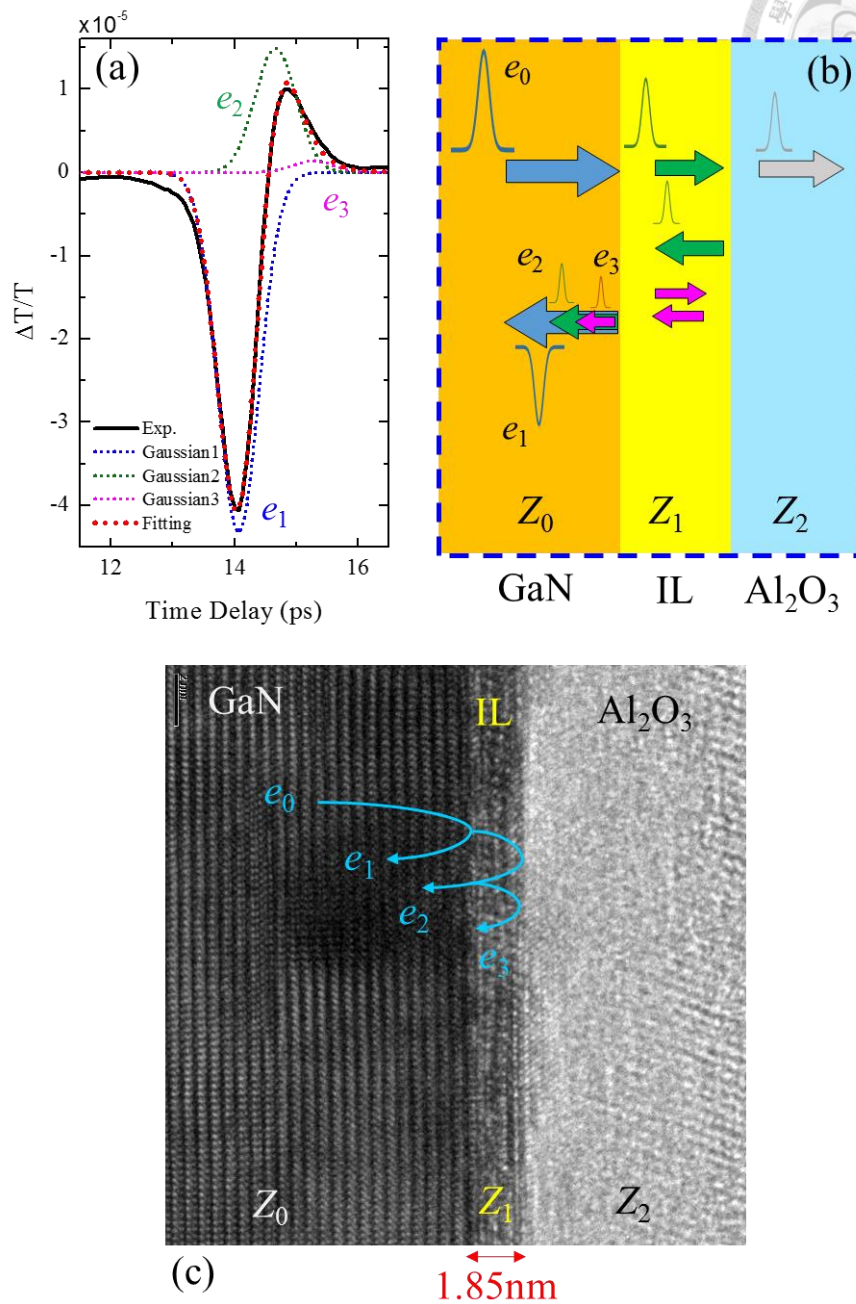
Fig. 3.7 (a) Zoom-in figure of the echo E1 with two fitted Gaussian pulses. e_1 (blue dash) denoted the echo reflected from GaN/IL interface and e_2 (green dash) denoted the one from IL/Al$_2$O$_3$ interface. The combination of e_1 and e_2 (red dot) was in good agreement with experimental data (black solid). (b) Zoom-in schematic diagram of the IL model system. (c) TEM picture of our IL model system with echo illustration. Z_0, Z_1, Z_2 are the characteristic acoustic impedances of GaN, IL, and Al$_2$O$_3$, respectively.
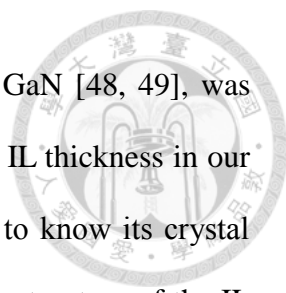
It is important to note that, in the calculation, we ignored the frequency-dependent diffusive scattering of acoustic phonons due to the interface roughness, since it would not significant affect our result. Roughness is indeed a critical issue, however, it's beyond the scope in this thesis, where we mainly aims at demonstrating transmission affected by an IL with a different elastic property. Besides, the acoustic attenuation inside the IL was also neglected for such a thin thickness. Nevertheless, in the following content, we would first present the value of Z_1 in a calculation neglecting diffusive scattering and acoustic attenuation; then, another value taking into account both neglected effects would be shown in the next section (**3.3 Discussion**) for comparison.

The sound velocity and mass density of GaN was 7.96 nm/ps and 6.095 g/cm^3, respectively. The sound velocity of 8.7 nm/ps in the Al$_2$O$_3$ film was obtained from our femtosecond acoustic A-scan data and the TEM image, while the mass density of 3.1 g/cm^3 was taken from the reported result in Ref. [47]. Solving Eqs. (3-5), we obtained the acoustic impedance of the IL between GaN and Al$_2$O$_3$ film to be around 18.6×10^6 $kg \cdot m^{-2} s^{-1}$ or $Pa \cdot s \cdot m^{-1}$. Besides, from the time delay between the fitted echo e_1 and e_2, the sound velocity in the 1.85nm-thick IL was estimated to be 6.16 nm/ps. Then, a mass density of 3.01 g/cm^3 was also obtained. Having mass density and sound velocity attained, we further evaluated the elastic constant of the IL in the cross-plane direction through the relation [32]

$$C = \rho \cdot V^2 \,, \qquad \qquad \text{Eq. (3-5)}$$

where ρ is the mass density and V is the longitudinal sound velocity of the IL.

The calculated cross-plane elastic constant of the IL was 114±1.4 GPa, where the error bar was estimated from the experimental noise in the time-domain trace. This value,

only about one-fourth of the elastic constant along c-axis (C_{33}) in GaN [48, 49], was interestingly lower than that of the material on either side. Since the IL thickness in our case is too small for nano-beam diffraction measurement, it's hard to know its crystal structure. In a thicker IL case reported by Ching-Chich Leu [50], the structure of the IL in a $SrBi_2Ta_2O_9$–Pt–Ti ferroelectric capacitor was revealed to be nanocrystalline. Gleiter [51] had in theory showed that nanocrystallines would have lower elastic modulus than their crystalline counterparts. Therefore, it could be possible that the IL in our case was also nanocrystalline and led to a lower elastic constant value. Besides, Clément Rossignol *et al.* had measured the longitudinal effective elastic constant in a permalloy/Al_2O_3 multilayer thin film. They reported the reduction of elastic constant with increasing multilayer period number while maintaining the total thickness [52]. Since the number of interfaces would increase with the period number, we think the result could also imply a softer interfacial layer between every permalloy/Al_2O_3 interface in their system. Therefore, the lower elastic constant revealed in our IL might not be unreasonable. We further suggested that other possible reasons may be the diffusion of oxygen into GaN or the substitution of nitride by oxygen during ALD process, which would impair the original compact structure of GaN at the interface.

Some values of the elastic constant, longitudinal sound velocity and mass density for several common oxides or semiconductors were listed in Table.3.1. To be clear, the value was chosen in the direction along c-axis if the material is crystalline.
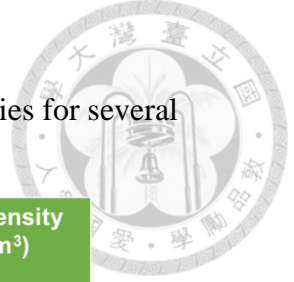
Table 3.1

Elastic constants, longitudinal sound velocities and mass densities for several semiconductors and oxides

	Elastic Constant (GPa)	Longitudinal Sound Velocity (nm/ps)	Mass density (g/cm³)
Al_2O_3 (Sapphire)	C_{33}= 498	10.9	4.1
Al_2O_3(amorphous)	272	8.7 [this work]	3.1
SiO_2 (α-quartz)	C_{33}= 107	6.32	2.66
SiO_2 (vitreous)	76	5.75	2.2
ZnO	C_{33}= 211	6	5.6
GaO_xN_y	114 [this work]	6.16 [this work]	3.01
GaN (Wurtzite)	C_{33}= 430	7.95	6.09
AlN	C_{33}= 457	10.1	4.47
InN	C_{33}= 200	5.8	6.81

(Note that the IL between GaN/Al_2O_3 are usually perceived as unsaturated gallium oxide GaO_x, or gallium oxynitride GaO_xN_y, here we used the latter notation)

The main reasons that we were able to analyze the elastic properties of an atomically-thin IL (see Fig.3.7 (c), the IL was only several atoms in thickness) are twofold: (i) the high spatial and temporal resolution and (ii) the coherent nature of our probing source.

Thanks to ultrashort femtosecond laser pulses and a narrow SQW optical piezoelectric transducer, we generated acoustic pulses with a spatial width ~3nm. Moreover, the resolution could be higher in materials with lower sound velocity than GaN, since the ratio of spatial width and sound velocity shall approximately maintain the same. Take the values in our case for example, the acoustic pulse width inside the IL should be around

$$6.16(nm/ps) \times \frac{3(nm)}{7.96(nm/ps)} \approx 2.31(nm).$$

As a matter of fact, we could resolve thickness that is even thinner than this value with convolution fittings, as already demonstrated in our successful probing of a 1.85nm-thick layer. We suggested this was an example of probing an IL amid two

heterogeneous solids, and we believed even higher resolution could be achieved with finer settings (e.g. delay stage and lock-in sampling rate) and more sophisticated fitting algorithms.

3.3 Further Discussion

3.3.1 Interface Roughness and Acoustic Attenuation

In previous section, we had estimated the acoustic impedance Z_1 of the interfacial layer (IL) while neglecting two factors that might influence the amplitudes of our femtosecond acoustic pulses: (i) the scattering at the boundaries due to interface roughness[53], and (ii) acoustic attenuation inside the 1.85nm-thick IL. In this section, we recalculated Z_1 under consideration of both effects, and the parameters we used were described below:

(i) For the roughness values of the two interfaces in our IL model system:

Using atom force microscopy (AFM), we had measure the roughness of bare GaN surface before the growth of Al_2O_3 film to be 0.25 nm. As shown in Fig. 3.8, if we assumed that the surface morphology do not change much while growing Al_2O_3 film, this value gave us an estimation of the interface roughness between IL and Al_2O_3 (red dash line). On the other hand, after femtosecond acoustic experiment, we etched out both Al_2O_3 film and the IL by buffered hydrofluoric acid (BHF) and measured the roughness of the remaining GaN surface to be 0.3 nm. This value shall give us another estimation of roughness for the GaN/IL interface in our system (green dash line).

(ii) For the acoustic attenuation:

Since many suggested the formation of the IL was due to the para-oxidation of the substrate, we used the acoustic attenuation value of a common oxide[54] as an example to show the influence of attenuation in an IL of such thin thickness.
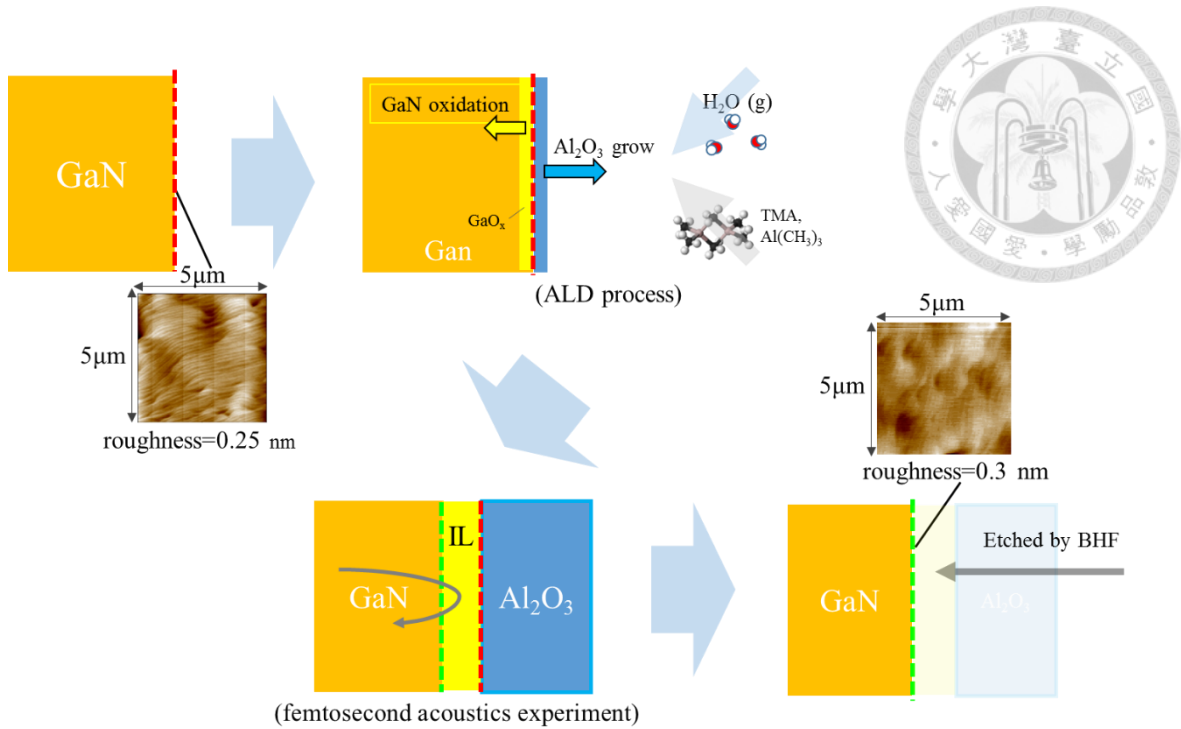
Fig. 3.8 The measurement of interface roughness in our IL model system. The roughness of IL/Al$_2$O$_3$ interface was assumed as the value measured before the growth of Al$_2$O$_3$ film (red dash). The roughness of GaN/IL

Under consideration of roughness scattering and acoustic attenuation, the new value of the acoustic impedance Z_1 obtained is $17.7 \times 10^6 \, kg \cdot m^{-2} s^{-1}$. Compared to the value of $18.6 \times 10^6 \, kg \cdot m^{-2} s^{-1}$ calculated while ignoring both effects, the difference was only ~5%. The reason for a decreased value instead of an increased one was suggested to because a larger mismatch in acoustic impedance was needed for an underestimated reflection of acoustic pulse due to roughness and attenuation. The comparison of fittings with/without considering roughness and attenuation was shown in figure 3.9, both revealed good agreements with the experimental data.
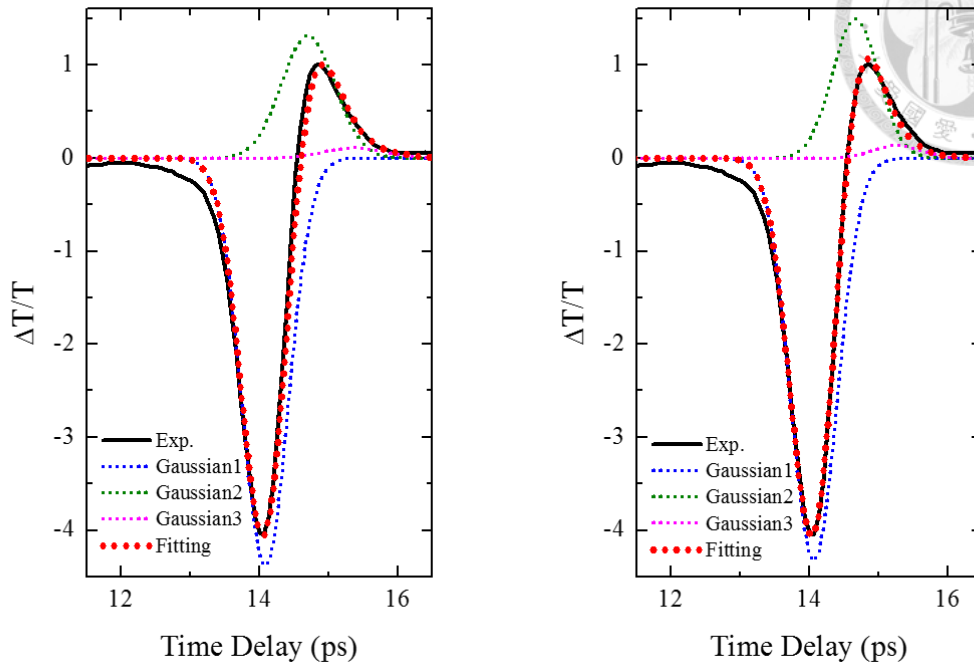
Fig. 3.9 Comparison of echo fittings with (left) and without (right) consideration of roughness scattering and acoustic attenuation.

3.3.2 Thermal Energy Transmission Reduction

In this section, we are going to calculate the thermal energy transmission with and without the interfacial layer (IL). It should be noted that the frequency spectrum of our femtosecond acoustic phonon pulses is ranging from 0~1.5 THz, which actually correspond to the dominate phonons below the temperature of 16.6K[55]. Even though, through the calculation, we could see how an IL would affect the thermal propagation between two materials, and recall our main concern in Chapter 1 that such an IL might hinder heat dissipation and restrict performance of advanced nano-devices. Here again we do not consider the frequency-dependent diffusive scattering at the boundaries. It is indeed another issue, however, it is in not our chief scope of this thesis. We just exhibit the thermal transmission changes in a simple but critical example with and without the IL.

Heat is mainly carried by incoherent acoustic phonons, thus in the calculation we do not consider the interference effect like in the previous section. The power (or energy) transmission coefficient is empolyed in this section [32, 56, 57]. For the case without an IL, the energy transmission coefficient from material 0 to material 2 is simply

$$T_{02} = \frac{4Z_0 Z_2}{(Z_0 + Z_2)^2}.$$

<div align="right">Eq. (3-6)</div>
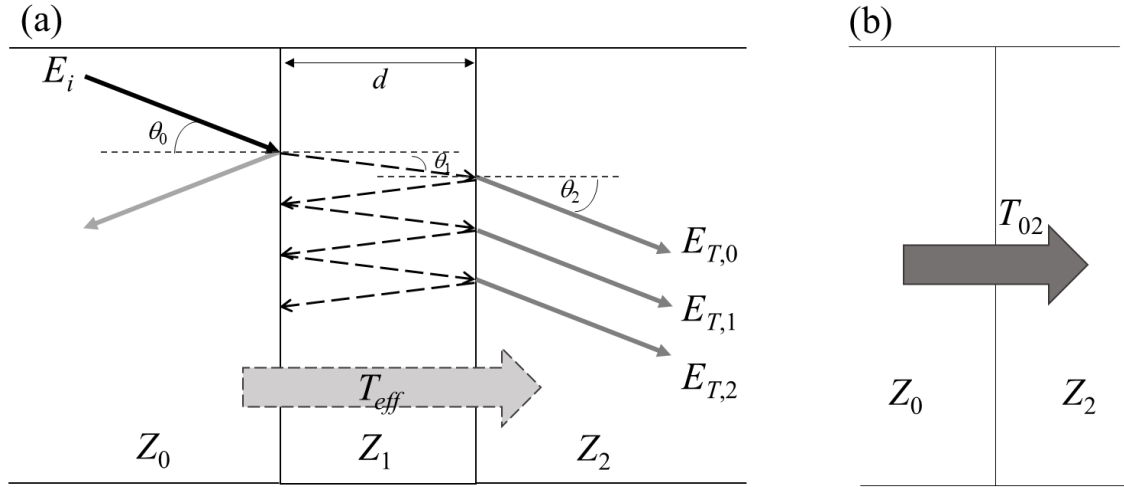
Fig. 3.10 Illustrative diagram for the calculation of energy transimission (a) with and (b) without the introduction of an interfacial layer.

For the case with an IL, let's first consider a portion of phonon energy E_i arriving at an incident angle θ_0 at the interface between material 0 and material 1. As illustrated in Fig.3.10 (a), $E_{T,n}$ represents the phonon energy transmitted through the IL after n-times additional roundtrip inside. In fact, each of them could be denoted using E_i as below:

$$E_{T,0} = T_{01}(\theta_1) T_{12}(\theta_1) \cdot e^{-\alpha_1 \left(\frac{d_1}{\cos\theta_1}\right)} \cdot E_i$$

$$E_{T,1} = T_{01}(\theta_1) T_{12}(\theta_1) [1 - T_{01}(\theta_1)][1 - T_{12}(\theta_1)] \cdot e^{-\alpha_1 \left(\frac{3d_1}{\cos\theta_1}\right)} \cdot E_i$$

$$E_{T,2} = T_{01}(\theta_1) T_{12}(\theta_1) [1 - T_{01}(\theta_1)]^2 [1 - T_{12}(\theta_1)]^2 \cdot e^{-\alpha_1 \left(\frac{5d_1}{\cos\theta_1}\right)} \cdot E_i$$

…

<div align="right">Eqs. (3-7)</div>

where α_1 is the attenuation coefficient in the IL, d_1 is the thickness of IL, and T_{01} and T_{12} are transmission coefficients between M0/M1 and M1/M2, repectively.

The effecitve energy transmission coefficient is obtain by summing all the transmitted energies in Eqs.(3-6), which is expressed as:

$$T_{eff} = \frac{\sum_n E_{T,n}}{E_i}$$

$$= \frac{T_{01}(\theta)T_{12}(\theta)e^{-\alpha_1 \cdot \left(\frac{d_1}{\cos\theta_1}\right)}}{1-[1-T_{01}(\theta)][1-T_{12}(\theta)]e^{-\alpha_1 \cdot \left(\frac{2d_1}{\cos\theta_1}\right)}} . \qquad \text{Eq. (3-8)}$$

In a normal incidence scheme and in the case that IL thickness is small enough, we can ignore the angle dependance and the attenuation term. T_{eff} thus become

$$T_{eff} = \frac{T_{01}T_{12}}{T_{01}+T_{12}-T_{01}T_{12}}$$

$$= \frac{16Z_0Z_1^2Z_2}{4Z_1Z_2(Z_0^2+Z_1^2)+4Z_0Z_1(Z_1^2+Z_2^2)} . \qquad \text{Eq. (3-9)}$$

With the impedance value of the IL (Z_1) obtained in section 3.3.2, the effective energy transmission coefficient calculated using Eq. (3-9) is 0.770 while the value will be 0.918 in the absence of the IL. Hence, a reduction of 16% in phonon energy transmission is caused by the formation of an IL in our demonstrated case.

The acoustic impedance of the IL, Z_1, is lower than Z_0 and Z_2, and the phonon energy transmission was reduced. It then occurred to us that how would the effective transmission coefficient be for other cases of Z_1. Therefore, we plotted the effective transmission (T_{eff}) as a function of Z_1, using Eq. (3-9) with given Z_0 and Z_2, as depicted in Fig. 3.11. The transmission coefficient (T_{02}) without the IL calculated from Eq. (3-6) was also shown as the red line in the figure for comparison. Trivially, the values of Z_1 at the two intersections in the figure were just Z_0 and Z_2, since either case would lead to a simple bi-material system for acoustic phonons. Besides, it was worth noting that T_{eff}

would exceed T_{02} when Z_1 lay between Z_2 and Z_0. This is actually not surprising, since the IL would act as an impedance matching layer when its impedance was between those of both sides[32]. Note that this part of discussion may imply the fact that the mechanical properties of materials should also be considered as a trade-off between those electronic ones (e.g. permittivity, carrier mobility, etc.), since a better heat dissipation would enhance device reliability and performance as well.
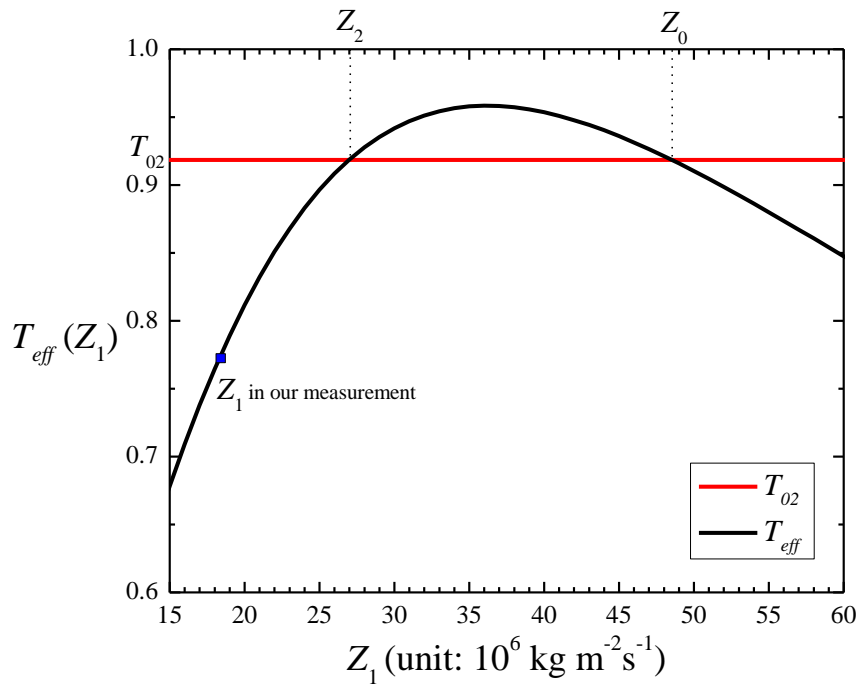
Fig. 3.11 Effective transmission (T_{eff}) of phonon energy through an IL as a function of the acoustic impedance of the IL, Z_1, using Eq. (3-9) (black). The transmission coefficient T_{02} without the IL was also plotted for reference (red). We used those values in our experiment for the plotting, where Z_0=48.5, Z_2=26.9 (unit: 10^6 kg m^{-2}s^{-1}) as previously discussed.
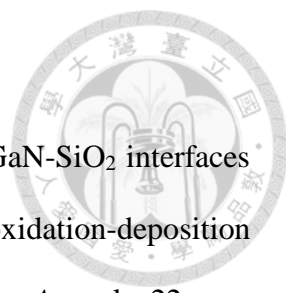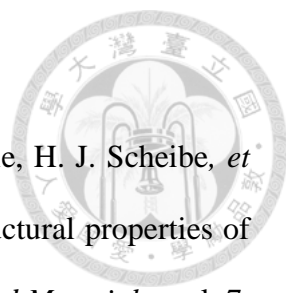
Chapter 4   Summary

In this thesis, we designed an interfacial layer (IL) model system between bulk GaN and Al_2O_3 film, and conducted femtosecond acoustic measurement to obtain the mechanical properties of the IL. A femtosecond acoustic pulse with a FWHM ~500fs was generated from a single quantum well (SQW) optical piezoelectric transducer (OPT) and serves as our probing source for the IL. With careful discussion and removing of the background signal in our experimental data, we obtained a clear femtosecond acoustic A-scan of our model system. Next, using convolution fitting algorithm on the first echo E1, we successfully estimated the acoustic impedance of the IL to be $18.6 \times 10^6 \, kg \cdot m^{-2} s^{-1}$. Then, a mass density of 3.01 g/cm^3 and a cross-plane elastic constant of 114 GPa for the IL were also obtained. The low value of the mass density might be the results of oxygen diffusion and substitution at the GaN/Al_2O_3 boundary, which also lead to a lower elastic constant than C_{33} along the c-axis in GaN. We further discussed the theoretical reduction in thermal energy transmission due to the existence of the IL, in order to recall our main concern in the beginning of the thesis. A reduction of 16% was evaluated through the calculations. Moreover, another possible scenario for the existence of the IL as the role of an impedance matching layer was also discussed. Most important of all, being capable of probing the elastic properties across layers of only several atoms thick, our technique could be perceived as the first step to deal with heat dissipation issue stemming from the ILs. Hopefully, our approach will provide a better thermal management for nano-scaled devices in the future.
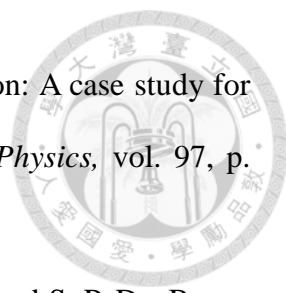
References

[1]   P. K. Schelling, L. Shi, and K. E. Goodson, "Managing heat for electronics," *Materials Today,* vol. 8, pp. 30-35, Jun 2005.

[2]   A. L. Moore and L. Shi, "Emerging challenges and materials for thermal management of electronics," *Materials Today,* vol. 17, pp. 163-174, May 2014.

[3]   G. E. Moore, "Progress in digital integrated electronics," in *Electron Devices Meeting, 1975 International*, 1975, pp. 11-13.

[4]   S. Banerjee, B. Shen, I. Chen, J. Bohlman, G. Brown, and R. Doering, "Conduction Mechanisms in Sputtered Ta_2O_5 on Si with an Interfacial SiO_2 Layer," *Journal of Applied Physics,* vol. 65, pp. 1140-1146, Feb 1 1989.

[5]   M. H. Cho, D. H. Ko, Y. G. Choi, K. Jeong, I. W. Lyo, D. Y. Noh*, et al.*, "Structural and electrical characteristics of Y_2O_3 films grown on oxidized Si(100) surface," *Journal of Vacuum Science & Technology a-Vacuum Surfaces and Films,* vol. 19, pp. 192-199, Jan-Feb 2001.

[6]   G. D. Wilk, R. M. Wallace, and J. M. Anthony, "High-κ gate dielectrics: Current status and materials properties considerations," *Journal of Applied Physics,* vol. 89, p. 5243, 2001.

[7]   M. H. Cho, Y. S. Roh, C. N. Whang, K. Jeong, S. W. Nahm, D. H. Ko*, et al.*, "Thermal stability and structural characteristics of HfO_2 films on Si (100) grown by atomic-layer deposition," *Applied Physics Letters,* vol. 81, pp. 472-474, Jul 15 2002.

[8]   M. Gutowski, J. E. Jaffe, C.-L. Liu, M. Stoker, R. I. Hegde, R. S. Rai*, et al.*, "Thermodynamic stability of high-K dielectric metal oxides ZrO_2 and HfO_2 in contact with Si and SiO_2," *Applied Physics Letters,* vol. 80, pp. 1897-1899,
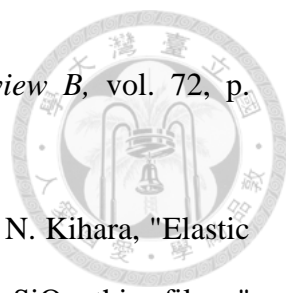
2002.

[9]   C. Bae and G. Lucovsky, "Low-temperature preparation of GaN-SiO$_2$ interfaces with low defect density. I. Two-step remote plasma-assisted oxidation-deposition process," *Journal of Vacuum Science & Technology A,* vol. 22, pp. 2402-2410, 2004.

[10]   FanY, K. J. Smith, LupkeG, A. T. Hanbicki, GoswamiR, C. H. Li*, et al.*, "Exchange bias of the interface spin system at the Fe/MgO interface," *Nat Nano,* vol. 8, pp. 438-444, 2013.

[11]   T. L. Duan, J. S. Pan, and D. S. Ang, "Interfacial chemistry and valence band offset between GaN and Al$_2$O$_3$ studied by X-ray photoelectron spectroscopy," *Applied Physics Letters,* vol. 102, p. 201604, May 20 2013.

[12]   N. Nakagawa, H. Y. Hwang, and D. A. Muller, "Why some interfaces cannot be sharp," *Nat Mater,* vol. 5, pp. 204-209, 2006.

[13]   N. Ashcroft and D. Mermin, *Solid State Physics*: Thomson Learning, 1976.

[14]   A. McGaughey and M. Kaviany, "Phonon transport in molecular dynamics simulations: Formulation and thermal conductivity prediction," in *Advances in Heat Transfer*. vol. 39, ed: Elsevier, 2006, pp. 169-255.

[15]   D. P. Sellan, E. S. Landry, J. E. Turney, A. J. H. McGaughey, and C. H. Amon, "Size effects in molecular dynamics thermal conductivity predictions," *Physical Review B,* vol. 81, p. 214305, Jun 21 2010.

[16]   X. D. Li and B. Bhushan, "A review of nanoindentation continuous stiffness measurement technique and its applications," *Materials Characterization,* vol. 48, pp. 11-36, Feb 2002.

[17]   Y. I. Golovin, "Nanoindentation and mechanical properties of solids in submicrovolumes, thin near-surface layers, and films: A Review," *Physics of the*

Solid State, vol. 50, pp. 2205-2236, 2008/12/01 2008.

[18]   D. Schneider, C. F. Meyer, H. Mai, B. Schöneich, H. Ziegele, H. J. Scheibe, *et al.*, "Non-destructive characterization of mechanical and structural properties of amorphous diamond-like carbon films," *Diamond and Related Materials,* vol. 7, pp. 973-980, 1998.

[19]   Q. Zhang, X. Xiao, Y.-T. Cheng, and M. W. Verbrugge, "A non-destructive method for measuring the mechanical properties of ultrathin films prepared by atomic layer deposition," *Applied Physics Letters,* vol. 105, p. 061901, 2014.

[20]   D. Schneider, T. Witke, T. Schwarz, B. Schoneich, and B. Schultrich, "Testing ultra-thin films by laser-acoustics," *Surface & Coatings Technology,* vol. 126, pp. 136-141, Apr 24 2000.

[21]   R. Pastorelli, A. C. Ferrari, M. G. Beghi, C. E. Bottani, and J. Robertson, "Elastic constants of ultrathin diamond-like carbon films," *Diamond and Related Materials,* vol. 9, pp. 825-830, Apr-May 2000.

[22]   "Surface acoustic waves and elastic constants of InN epilayers determined by Brillouin scattering," *physica status solidi (RRL) - Rapid Research Letters,* vol.6, issue6, 256-258, 2012.

[23]   A. B. Baggeroer, W. A. Kuperman, and P. N. Mikhalevsky, "An Overview of Matched-Field Methods in Ocean Acoustics," *Ieee Journal of Oceanic Engineering,* vol. 18, pp. 401-424, Oct 1993.

[24]   M. Culjat, R. S. Singh, D. C. Yoon, and E. R. Brown, "Imaging of human tooth enamel using ultrasound," *IEEE Trans Med Imaging,* vol. 22, pp. 526-9, Apr 2003.

[25]   H.-C. Wang, S. Fleming, Y.-C. Lee, M. Swain, S. Law, and J. Xue, "Laser ultrasonic evaluation of human dental enamel during remineralization

treatment," *Biomedical Optics Express,* vol. 2, pp. 345-355, 2011/02/01 2011.

[26] S. Popovics, J. L. Rose, and J. S. Popovics, "The behaviour of ultrasonic pulses in concrete," *Cement and Concrete Research,* vol. 20, pp. 259-270, 1990.

[27] K. H. Lin, G. W. Chern, C. T. Yu, T. M. Liu, C. C. Pan, G. T. Chen*, et al.*, "Optical piezoelectric transducer for nano-ultrasonics," *IEEE Trans Ultrason Ferroelectr Freq Control,* vol. 52, pp. 1404-14, Aug 2005.

[28] S. F. Chichibu, A. C. Abare, M. P. Mack, M. S. Minsky, T. Deguchi, D. Cohen*, et al.*, "Optical properties of InGaN quantum wells," *Materials Science and Engineering B-Solid State Materials for Advanced Technology,* vol. 59, pp. 298-306, May 6 1999.

[29] C. W. Chern, C. K. Sun, G. D. Sanders, and C. J. Stanton, "Generation of Coherent Acoustic Phonons in Nitride-Based Semiconductor Nanostructures," in *Ultrafast Dynamical Processes in Semiconductors*, K.-T. Tsen, Ed., 1 ed New York: Springer, 2004, pp. 339-394.

[30] D. A. B. Miller, D. S. Chemla, and S. Schmittrink, "Relation between Electroabsorption in Bulk Semiconductors and in Quantum-Wells - the Quantum-Confined Franz-Keldysh Effect," *Physical Review B,* vol. 33, pp. 6976-6982, May 15 1986.

[31] G. W. Chern, K. H. Lin, and C. K. Sun, "Transmission of light through quantum heterostructures modulated by coherent acoustic phonons," *Journal of Applied Physics,* vol. 95, pp. 1114-1121, Feb 1 2004.

[32] D. Royer and E. Dieulesaint, *Elastic Waves in Solids I: Free and Guided Propagation*, 1 ed.: Springer-Verlag Berlin Heidelberg, 2000.

[33] S. M. George, "Atomic Layer Deposition: An Overview," *Chemical Reviews,* vol. 110, pp. 111-131, 2010/01/13 2010.

[34] R. L. Puurunen, "Surface chemistry of atomic layer deposition: A case study for the trimethylaluminum/water process," *Journal of Applied Physics,* vol. 97, p. 121301, 2005.

[35] C. K. Sun, S. Keller, G. Wang, M. S. Minsky, J. E. Bowers, and S. P. DenBaars, "Radiative recombination lifetime measurements of InGaN single quantum well," *Applied Physics Letters,* vol. 69, pp. 1936-1938, 1996.

[36] C.-K. Sun, F. Vallée, S. Keller, J. E. Bowers, and S. P. DenBaars, "Femtosecond studies of carrier dynamics in InGaN," *Applied Physics Letters,* vol. 70, pp. 2004-2006, 1997.

[37] J. Shah, *Ultrafast Spectroscopy of Semiconductors and Semiconductor Nanostructures*: Springer-Verlag Berlin Heidelberg, 1999.

[38] C. Thomsen, H. T. Grahn, H. J. Maris, and J. Tauc, "Surface generation and detection of phonons by picosecond light pulses," *Physical Review B,* vol. 34, pp. 4129-4138, 09/15/ 1986.

[39] C.-K. Sun, J.-C. Liang, C. J. Stanton, A. Abare, L. Coldren, and S. P. DenBaars, "Large coherent acoustic-phonon oscillation observed in InGaN/GaN multiple-quantum wells," *Applied Physics Letters,* vol. 75, pp. 1249-1251, 1999.

[40] C. K. Sun, J. C. Liang, and X. Y. Yu, "Coherent acoustic phonon oscillations in semiconductor multiple quantum wells with piezoelectric fields," *Phys Rev Lett,* vol. 84, pp. 179-82, Jan 3 2000.

[41] A. Devos and R. Côte, "Strong oscillations detected by picosecond ultrasonics in silicon: Evidence for an electronic-structure effect," *Physical Review B,* vol. 70, p. 125208, 09/23/ 2004.

[42] R. Liu, G. D. Sanders, C. J. Stanton, C. S. Kim, J. S. Yahng, Y. D. Jho*, et al.*, "Femtosecond pump-probe spectroscopy of propagating coherent acoustic

phonons in $In_xGa_{1-x}N/GaN$ heterostructures," *Physical Review B,* vol. 72, p. 195335, 11/23/ 2005.

[43] H. Ogi, T. Shagawa, N. Nakamura, M. Hirao, H. Odaka, and N. Kihara, "Elastic constant and Brillouin oscillations in sputtered vitreous SiO_2 thin films," *Physical Review B,* vol. 78, 2008.

[44] C. Thomsen, H. T. Grahn, H. J. Maris, and J. Tauc, "Picosecond interferometric technique for study of phonons in the brillouin frequency range," *Optics Communications,* vol. 60, pp. 55-58, 10/15/ 1986.

[45] G. Yu, G. Wang, H. Ishikawa, M. Umeno, T. Soga, T. Egawa*, et al.*, "Optical properties of wurtzite structure GaN on sapphire around fundamental absorption edge (0.78–4.77 eV) by spectroscopic ellipsometry and the optical transmission method," *Applied Physics Letters,* vol. 70, p. 3209, 1997.

[46] A. Polian, M. Grimsditch, and I. Grzegory, "Elastic constants of gallium nitride," *Journal of Applied Physics,* vol. 79, pp. 3343-3344, Mar 15 1996.

[47] M. D. Groner, F. H. Fabreguette, J. W. Elam, and S. M. George, "Low-temperature Al_2O_3 atomic layer deposition," *Chemistry of Materials,* vol. 16, pp. 639-645, Feb 24 2004.

[48] O. Ambacher, "Growth and applications of Group III nitrides," *Journal of Physics D-Applied Physics,* vol. 31, pp. 2653-2710, Oct 21 1998.

[49] W. Soluch, E. Brzozowski, M. Lysakowska, and J. Sadura, "Determination of mass density, dielectric, elastic, and piezoelectric constants of bulk GaN crystal," *Ultrasonics, Ferroelectrics, and Frequency Control, IEEE Transactions on,* vol. 58, pp. 2469-2474, 2011.

[50] C.-C. Leu, "Nanocrystalline Pt interfacial layer formed by stress in a $SrBi_2Ta_2O_9$–Pt–Ti ferroelectric capacitor," *Journal of Materials Research,* vol.

22, pp. 1718-1725, 2011.

[51] H. Gleiter, "Nanocrystalline materials," *Progress in Materials Science,* vol. 33, pp. 223-315, 1989.

[52] C. Rossignol, B. Perrin, B. Bonello, P. Djemia, P. Moch, and H. Hurdequint, "Elastic properties of ultrathin permalloy/alumina multilayer films using picosecond ultrasonics and Brillouin light scattering," *Physical Review B,* vol. 70, Sep 2004.

[53] Y. C. Wen, C. L. Hsieh, K. H. Lin, H. P. Chen, S. C. Chin, C. L. Hsiao*, et al.*, "Specular scattering probability of acoustic phonons in atomically flat interfaces," *Phys Rev Lett,* vol. 103, p. 264301, Dec 31 2009.

[54] Y. C. Wen, S. H. Guol, H. P. Chen, J. K. Sheu, and C. K. Sun, "Femtosecond ultrasonic spectroscopy using a piezoelectric nanolayer: Hypersound attenuation in vitreous silica films," *Applied Physics Letters,* vol. 99, p. 051913, Aug 1 2011.

[55] D. G. Cahill and R. O. Pohl, "Lattice-Vibrations and Heat-Transport in Crystals and Glasses," *Annual Review of Physical Chemistry,* vol. 39, pp. 93-121, 1988.

[56] E. Swartz and R. Pohl, "Thermal boundary resistance," *Reviews of Modern Physics,* vol. 61, pp. 605-668, 1989.

[57] Z. Liang, K. Sasikumar, and P. Keblinski, "Thermal Transport across a Substrate －Thin-Film Interface: Effects of Film Thickness and Surface Roughness," *Physical Review Letters,* vol. 113, p. 065901, 08/08/ 2014.